GEOPHYSICS, VOL. 85, NO. 4 (JULY-AUGUST 2020); P. KS127–KS138, 16 FIGS.
10.1190/GEO2019-0311.1

Source location with cross-coherence migration

Yujin Liu[1], Yue Ma[1], and Yi Luo[2]

ABSTRACT

Locating microseismic source positions using seismic energy emitted from hydraulic fracturing is essential for choosing optimal fracking parameters and maximizing the fracturing effects in hydrocarbon exploitation. Interferometric crosscorrelation migration (ICCM) and zero-lag autocorrelation of time-reversal imaging (ATRI) are two important passive seismic source locating approaches that are proposed independently and seem to be substantially different. We have proven that these two methods are theoretically identical and produce very similar images. Moreover, we have developed cross-coherence that uses normalization by the spectral amplitude of each of the traces, rather than crosscorrelation or deconvolution, to improve the ICCM and ATRI methods. The adopted method enhances the spatial resolution of the source images and is particularly effective in the presence of highly variable and strong additive random noise. Synthetic and field data tests verify the equivalence of the conventional ICCM and ATRI and the equivalence of their improved versions. Compared with crosscorrelation- and deconvolution-based source locating methods, our approach shows a high-resolution property and antinoise capability in numerical tests using synthetic data with single and multiple sources, as well as field data.

INTRODUCTION

Source locations of passive seismicity induced by fluid injection during fracturing provide important information on deformation, fluid movement, and the geomechanical condition of hydrocarbon reservoirs (Maxwell et al., 2010; Shapiro, 2015). Source locations usually are determined by ray-based methods using picked arrival times and a given velocity model (Pujol, 2004). For example, the double-difference method estimates the source locations by minimizing the residuals between the theoretical and observed traveltime differences for pairs of earthquakes at each station while linking together all observed event-station pairs (Waldhauser and Ellsworth, 2000; Zhang and Thurber, 2003). For these methods, arrival-time picking is an inevitable step and can be performed manually or automatically. The hand picking process is tedious, labor intensive, vulnerable to human biases, and time-consuming. Auto-picking algorithms may struggle to produce reliable pickings for low signal-to-noise ratio (S/N) data sets or those with complicated phases. Several waveform-based source imaging methods without picking have been developed. Kao and Shan (2004) propose the source-scanning algorithm that identifies the spatial and temporal distribution of sources by systematically scanning through a range of trial source locations and origin times. This method does not need to pick arrival times of seismic phases accurately or to calculate synthetic seismograms but is computationally intensive.

Time-reversal imaging (TRI) is one of the most popular source-locating techniques that relies on the time-reversed extrapolation of the observed wavefields. The principle of TRI is that the extrapolated wavefields from receivers focus at the initial position of seismic sources given a reasonably accurate velocity model (McMechan, 1982; Gajewski and Tessmer, 2005; Fink, 2006). Douma et al. (2013) improve the temporal and spatial focusing of a microseismic event using deconvolution. The TRI method uses all receivers simultaneously without picking; thus, the S/N can be improved by increasing the number of receivers (Sava, 2011). Because the extrapolated receiver wavefields have four dimensions (time and 3D in space), we have to scan the entire 4D volume to find the location of the sources. Artman et al. (2010) consider the problem of location estimation as a migration problem, and the time axis collapses by incorporating zero-lag auto- and crosscorrelation imaging conditions (Claerbout, 1971). Witten and Shragge (2015, 2017a, 2017b) show how extended crosscorrelation imaging condition can be developed and used for P- and S-wave velocity model inversion on synthetic and field data. For acoustic media, the method proposed by Artman et al. (2010) is known as the zero-lag autocorrelation of time-reversal imaging (ATRI) method. It produces a low-resolution image with artifacts

Manuscript received by the Editor 15 May 2019; revised manuscript received 7 February 2020; published ahead of production 28 March 2020; published online 14 May 2020.

[1]Aramco Beijing Research Center, Aramco Asia, Beijing, China. E-mail: yujin.liu@aramcoasia.com; yue.ma@aramcoasia.com.
[2]EXPEC Advanced Research Center, Saudi Aramco, Dhahran, Saudi Arabia. E-mail: yi.luo@aramco.com.

when the number of receivers is insufficient. Nakata and Beroza (2016) and Sun et al. (2015) independently propose to apply multidimensional crosscorrelation to improve the spatial resolution of the source image. Because the crosscorrelation imaging condition requires wavefield propagation using data from each receiver separately, it is computationally intensive for wave-equation implementation. Sun et al. (2015) propose to apply the hybrid multiplicative TRI method to back-propagated wavefields computed from groups of receivers to mitigate this cost problem. Zhu et al. (2019) further detail the implementation of the hybrid multiplicative TRI method and show the failure of the crosscorrelation imaging condition in the presence of strong noise, but the hybrid imaging condition works satisfactorily. Sun et al. (2016) show that the time-reversal wavefield does not provide accurate amplitude and phase information of the passive source function because the time-reversal wavefield is modeled by the adjoint state equation, not exactly the inverse of the forward wave propagation. This problem can be addressed by the waveform-inversion method (Sun et al., 2016). Song et al. (2017) demonstrate that by estimating and applying a nonstationary filter (approximated Hessian) on the recorded data prior to back propagation, it can correct the illumination issues and provide a source image with better focusing. The spatial resolution of the source image can be improved further by adding a regularization term in the objective function of the waveform-inversion method to impose sparsity in space and smoothness in time on the source wavefield (Gao et al., 2017; Sharan et al., 2018; Li et al., 2019).

Another choice of locating seismic sources without picking is to use crosscorrelation as an interferometry method to reconstruct the impulse response of the first-arrival traveltime difference between receivers, then apply the crosscorrelation imaging condition to the back-projected wavefield to determine the source distribution (Schuster et al., 2004). For passive seismic data stimulated by a continuous source signature, such as the source generated by the drill-bit when it cracks the surrounding rocks, the crosscorrelation of traces can collapse the ring-like source wavelet into an impulse-like wavelet leading to a good spatial resolution compared to the original TRI method. Moreover, the ICCM method eliminates the need for a known excitation source time by generating the virtual shot gather. However, it limits the spatial resolution of the source image because the frequency spectra of source wavelets have been squared in the virtual shot gather after crosscorrelation. To enhance the resolution of the seismic source image, Wu et al. (2017) introduce deconvolution migration by combining deconvolution interferometry with interferometric crosscorrelation migration. Cao et al. (2012) propose to use the recorded band-limited Green's functions to focus the passive signal to the source location. This method has properties of high-resolution and super stacking because the multiple scattering events are utilized for the imaging. Li and Baan (2016) show that either pressure or particle displacement/velocity wavefields focus not only at the true event location but also on a false location by traditional reverse time extrapolation especially for limited borehole observation geometries. They develop representation-theorem-based reverse time extrapolation to mitigate the false ghost focusing. Moreover, they also introduce a new focusing criterion based on the Hough transform to better determine the origin time and hypocenter of recorded microseismic events. Zhao and Curtis (2019) propose a relative source location method based on coda-wave interferometry (Snieder et al., 2002) that uses multiple scattered waves. It has the advantages of insensitivity to velocity errors, the number of seismic stations, and source-to-station azimuth coverage. In the context of structure imaging using passive seismic reflection data, Artman (2006) demonstrates that the interferometric method is equivalent to the direct migration method. However, for source imaging, both interferometric and direct migration methods use transmission waves and there is no theoretical analysis of the relationship between these two methods.

In this paper, we first prove that the ICCM method is equivalent to the zero-lag ATRI method theoretically. Then, we propose another two alternatives based on cross-coherence to improve the resolution of the two mentioned methods. Unlike crosscorrelation, which is stable but needs estimation of the power spectrum of the noise source, and deconvolution, which is unstable and needs regularization, the cross-coherence method calculates the crosscorrelation of traces normalized by their spectral amplitudes in the frequency domain and therefore does not require estimation of the source spectrum (Nakata et al., 2011). The proposed methods generate the virtual shot gathers by applying cross-coherence between the master trace and all of the other traces in the observed data. All of the virtual shot gathers then are migrated and stacked together to generate the image of the source location. Similar to the ICCM and ATRI methods, we prove that the proposed two modified cross-coherence-based methods are also identical. Then, we use the synthetic and field data to numerically verify their equivalence. We also compare the proposed methods with conventional ICCM and deconvolution migration under different conditions including band-limited random noise, velocity perturbations, and multiple sources. Numerical tests demonstrate that the proposed methods improve the spatial resolution of the source image and are particularly effective and robust in the presence of highly variable and strong additive random noise.

THEORY

We first review the basic principles of ICCM and ATRI. Then, we prove the equivalence of these two methods. Finally, we propose the cross-coherence migration method and its equivalent implementation of the ATRI method.

Interferometric crosscorrelation migration

ICCM could be regarded as any algorithm that inverts correlated seismic data for the reflectivity or source distribution (Schuster et al., 2004). For identifying source locations, ICCM contains three steps: (1) generate the virtual shot gathers by crosscorrelating the master trace with all of the traces in the observed data, (2) migrate each of the virtual shot gathers to obtain a single-shot source image, and (3) stack all of these images together to obtain the final source image. To detail these three steps, let two frequency-domain traces at the locations $\mathbf{x}_i$ and $\mathbf{x}_j$ be denoted, respectively, by $D(\mathbf{x}_i, \omega)$ and $D(\mathbf{x}_j, \omega)$, $i, j = 1, \ldots, N$, where N is the number of receivers. Assuming that the Green's functions from source location $\mathbf{x}$ to the receivers at $\mathbf{x}_i$ and $\mathbf{x}_j$ are $G(\mathbf{x}_i, \mathbf{x}, \omega)$ and $G(\mathbf{x}_j, \mathbf{x}, \omega)$, respectively, the virtual shot gather at location $\mathbf{x}_i$ can be generated by crosscorrelating all of the traces at $\mathbf{x}_j$, $j = 1, \ldots, N$, with the trace fixed at $\mathbf{x}_i$ (referred to as the master trace), that is,

$$C(\mathbf{x}_j, \mathbf{x}_i, \omega) = D^*(\mathbf{x}_i, \omega) D(\mathbf{x}_j, \omega), \quad j = 1, \ldots, N. \quad (1)$$

To locate the subsurface source, only the crosscorrelation term of the direct wavefields (which are waves that travel from the physical source to receivers) is needed. If we ignore the amplitude spectra of input traces, $C(\mathbf{x}_j, \mathbf{x}_i, \omega)$ can be considered as the traveltime difference between the direct waves from the physical source $\mathbf{x}$ to receivers $\mathbf{x}_j$ and $\mathbf{x}_i$. The source image $I(\mathbf{x})$ can be obtained by migrating $C(\mathbf{x}_j, \mathbf{x}_i, \omega)$ and summing over all frequencies, receiver locations $\mathbf{x}_j$ and virtual shot locations $\mathbf{x}_i$:

$$I(\mathbf{x}) = \sum_i \sum_j \sum_\omega M(\mathbf{x}; \mathbf{x}_j, \mathbf{x}_i, \omega) C(\mathbf{x}_j, \mathbf{x}_i, \omega), \qquad (2)$$

where $M(\mathbf{x}; \mathbf{x}_j, \mathbf{x}_i, \omega)$ is the crosscorrelation migration kernel, which migrates the crosscorrelation result $C(\mathbf{x}_j, \mathbf{x}_i, \omega)$ to all possible source locations. It can be expressed using the Green's function

$$M(\mathbf{x}; \mathbf{x}_j, \mathbf{x}_i, \omega) = G(\mathbf{x}_i, \mathbf{x}, \omega) G^*(\mathbf{x}_j, \mathbf{x}, \omega). \qquad (3)$$

Considering only the traveltime information of the direct wave in the Green's function, equation 3 simplifies to

$$M(\mathbf{x}; \mathbf{x}_j, \mathbf{x}_i, \omega) = e^{-i\omega(t_{\mathbf{x}\mathbf{x}_i} - t_{\mathbf{x}\mathbf{x}_j})}, \qquad (4)$$

where $t_{\mathbf{x}\mathbf{x}_i}$ and $t_{\mathbf{x}\mathbf{x}_j}$ are the traveltime from source $\mathbf{x}$ to receivers $\mathbf{x}_i$ and $\mathbf{x}_j$, respectively. This migration kernel annihilates the traveltime difference $t_{\mathbf{x}\mathbf{x}_j} - t_{\mathbf{x}\mathbf{x}_i}$ when the trial source location $\mathbf{x}$ is on an isochron in 2D or an isochronous surface in 3D. For a 2D constant-velocity model, the isochron of the crosscorrelation migration is a hyperbola with foci at two receiver locations $\mathbf{x}_i$ and $\mathbf{x}_j$, where $\mathbf{x}_i$ is the closer fixed point.

To implement ICCM by wave-equation extrapolation operators, we first apply crosscorrelation to generate a virtual shot gather $C(\mathbf{x}_j, \mathbf{x}_i, \omega), j = 1, \ldots, N$, at the virtual shot location $\mathbf{x}_i$; second, we reconstruct the source wavefield $G^*(\mathbf{x}_i, \mathbf{x}, \omega)$ by back propagating a delta function at the virtual shot location $\mathbf{x}_i$; third, we reconstruct the receiver wavefield by back propagating the virtual shot gather $\sum_j G^*(\mathbf{x}_j, \mathbf{x}, \omega) C(\mathbf{x}_j, \mathbf{x}_i, \omega)$; then, we apply the zero-lag crosscorrelation image condition on the reconstructed source and receiver wavefields to generate the source image of a single virtual shot gather. The final source image is obtained by repeating the above steps through all of the N virtual shot locations and summing over all of the results.

In practice, the trace at the master trace location $\mathbf{x}_i$ and its neighbors are muted because the direct wave migration kernel in equations 3 and 4 has a zero or nearly zero phase when $\mathbf{x}_i \approx \mathbf{x}_j$. This is undesirable because any energy from those traces close to the master trace will be smeared uniformly throughout the model, not only at the true source location.

Zero-lag autocorrelation of time-reversal imaging

For time-reversal imaging, all of the recorded wavefields are propagated in reversed time. The propagated 4D wavefields in the frequency domain are expressed as

$$W(\mathbf{x}, \omega) = \sum_i G^*(\mathbf{x}_i, \mathbf{x}, \omega) D(\mathbf{x}_i, \omega), \qquad (5)$$

where the observed records at all receivers are backpropagated simultaneously; thus, the summation in the above equation is computed implicitly. Various imaging conditions can be applied to obtain the source image from the 4D wavefields. In this paper, we focus on the zero-lag autocorrelation imaging condition (Artman et al., 2010):

$$I(\mathbf{x}) = \sum_\omega W^*(\mathbf{x}, \omega) W(\mathbf{x}, \omega). \qquad (6)$$

To implement ATRI by wave-equation extrapolation operators, we first back propagate the data recorded at all of the receivers simultaneously (equation 5). Then, the zero-lag autocorrelation imaging condition (equation 6) is applied to obtain the source image.

Equivalence of ICCM and ATRI

Substituting equation 5 into 6, we obtain

$$I(\mathbf{x}) = \sum_\omega \sum_i G(\mathbf{x}_i, \mathbf{x}, \omega) D^*(\mathbf{x}_i, \omega) \sum_j G^*(\mathbf{x}_j, \mathbf{x}, \omega) D(\mathbf{x}_j, \omega). \qquad (7)$$

After interchanging the summation order, equation 7 becomes

$$I(\mathbf{x}) = \sum_i \sum_j \sum_\omega G(\mathbf{x}_i, \mathbf{x}, \omega) G^*(\mathbf{x}_j, \mathbf{x}, \omega) D^*(\mathbf{x}_i, \omega) D(\mathbf{x}_j, \omega). \qquad (8)$$

With the definition of crosscorrelation in equation 1 and the crosscorrelation migration kernel in equation 3, equation 8 is exactly the same as the ICCM equation 2. Therefore, we demonstrate that ATRI is equivalent to ICCM theoretically.

To illuminate the relationship between the ATRI and ICCM methods, Figure 1a and 1b depicts the basic principles of the ATRI and ICCM methods, respectively. Although these two methods produce identical results theoretically, their implementations and computational expenses are quite different. In the ICCM method, two back propagations are needed in the migration of a single virtual shot gather. There is a total of N virtual shot gathers; therefore, $2N$ times back propagations are needed for generating the final source image. In comparison, only a single back propagation of the original data is needed in the ATRI method. Usually, the ATRI method is more straightforward to apply and is more efficient than the ICCM method. However, in the case of passive seismic data generated by

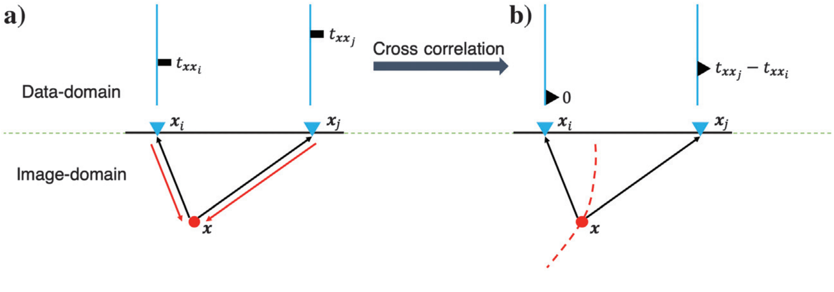

Figure 1. Schematics to illuminate the principles of (a) ATRI and (b) ICCM methods. The black arrows show the directions of forward wave propagation, and the red arrows show the directions of back propagation for imaging. The red dashed line shows the impulse response of crosscorrelation migration, which is a hyperbola in the case of a constant velocity medium.

a continuous source signature, it is challenging or even impossible to identify the first arrivals. Then, it might take a long computational time for a single backward propagation of the complete continuous data. It is worth noting that even though ATRI and ICCM are theoretically equivalent, the time lag truncation of crosscorrelation in the virtual shot gathers generation may cause minor differences between the ATRI and ICCM results.

Improvements to ICCM and ATRI

In the ICCM method, the virtual shot gathers are generated using the stable crosscorrelation. This process smears the source wavelet into a longer wavelet and blurs the final source image. Wu et al. (2017) demonstrate that using deconvolution, rather than crosscorrelation, to generate the virtual shot gathers can improve the resolution of the source image. This method is called deconvolution migration, and it can be expressed as

$$I(\mathbf{x})=\sum_{i}\sum_{j}\sum_{\omega}G(\mathbf{x}_i,\mathbf{x},\omega)G^*(\mathbf{x}_j,\mathbf{x},\omega)\frac{D^*(\mathbf{x}_i,\omega)D(\mathbf{x}_j,\omega)}{|D(\mathbf{x}_i,\omega)|^2}. \tag{9}$$

We use cross-coherence interferometry to generate the virtual shot gathers for source imaging. Cross-coherence calculates the crosscorrelation of traces normalized by their spectral amplitudes in the frequency domain (Aki, 1957). It uses the phase of each trace, ignoring amplitude information, for suppressing the influence of additive noise and overcomes problems resulting from amplitude variations among input traces (Nakata et al., 2011). Such a technique also is referred to as frequency equalization or spectral whitening. By combining the cross-coherence interferometry with ICCM, we propose cross-coherence migration, which can be expressed as

$$I(\mathbf{x})=\sum_{i}\sum_{j}\sum_{\omega}G(\mathbf{x}_i,\mathbf{x},\omega)G^*(\mathbf{x}_j,\mathbf{x},\omega)\frac{D^*(\mathbf{x}_i,\omega)D(\mathbf{x}_j,\omega)}{|D(\mathbf{x}_i,\omega)||D(\mathbf{x}_j,\omega)|}. \tag{10}$$

The implementation of equation 10 is similar to the conventional ICCM method (equation 8), except replacing the crosscorrelation with cross-coherence for generating the virtual shot gathers. Equation 10 can be rearranged as

$$I(\mathbf{x})=\sum_{\omega}\sum_{i}G(\mathbf{x}_i,\mathbf{x},\omega)\frac{D^*(\mathbf{x}_i,\omega)}{|D(\mathbf{x}_i,\omega)|}\sum_{j}G^*(\mathbf{x}_j,\mathbf{x},\omega)\frac{D(\mathbf{x}_j,\omega)}{|D(\mathbf{x}_j,\omega)|}. \tag{11}$$

The implementation of equation 11 is similar to the conventional ATRI method (equation 7), except that we back propagate the normalized input data $D(\mathbf{x}_i,\omega)/|D(\mathbf{x}_i,\omega)|$, rather than the original data $D(\mathbf{x}_i,\omega)$. Therefore, it shares the same computational cost as the conventional ATRI method. Similar to the relationship between conventional ICCM and ATRI methods, the cross-coherence migration (equation 10) and its corresponding ATRI implementation (equation 11) are theoretically equivalent as well. But their numerical results may have minor differences because of the time lag truncation of cross-coherence. Another possible origin of difference comes from the stability factors in the implementation of frequency-domain normalizations in equations 10 and 11. It is worth noting that Girard and Shragge (2020) use a similar approach that whitens ambient wavefield spectra, but for the purpose of subsurface structure imaging using passive seismic reflection waves.

The influences of amplitude variation among traces and additive noise

The difference between crosscorrelation migration (equation 8), deconvolution migration (equation 9), and cross-coherence migration (equation 10) is that they use three different methods to generate virtual shot gathers. The crosscorrelation C_{ij}, deconvolution D_{ij}, and cross-coherence H_{ij} of data records at locations $\mathbf{x}_i$ and $\mathbf{x}_j$ are

$$C_{ij}=D^*(\mathbf{x}_i,\omega)D(\mathbf{x}_j,\omega), \tag{12}$$

$$D_{ij}=\frac{D^*(\mathbf{x}_i,\omega)D(\mathbf{x}_j,\omega)}{|D(\mathbf{x}_i,\omega)|^2}, \tag{13}$$

$$H_{ij}=\frac{D^*(\mathbf{x}_i,\omega)D(\mathbf{x}_j,\omega)}{|D(\mathbf{x}_i,\omega)||D(\mathbf{x}_j,\omega)|}. \tag{14}$$

Assuming that there is only one passive source, the recorded data at receivers $\mathbf{x}_i$ and $\mathbf{x}_j$ can be described as

$$\begin{aligned}D(\mathbf{x}_i,\omega)&=W(\omega)G(\mathbf{x}_i,\omega)R(\mathbf{x}_i,\omega)\\&\quad+N(\mathbf{x}_i,\omega)\end{aligned} \tag{15}$$

and

$$\begin{aligned}D(\mathbf{x}_j,\omega)&=W(\omega)G(\mathbf{x}_j,\omega)R(\mathbf{x}_j,\omega)\\&\quad+N(\mathbf{x}_j,\omega),\end{aligned} \tag{16}$$

respectively. In equations 15 and 16, $W(\omega)$ is the source wavelet; $G(\mathbf{x}_i,\omega)$ and $G(\mathbf{x}_j,\omega)$ are the Green's functions at the receivers $\mathbf{x}_i$ and $\mathbf{x}_j$; $R(\mathbf{x}_i,\omega)$ and $R(\mathbf{x}_j,\omega)$ are the receiver-ground-coupling functions used to describe the variations in amplitude, time, phase, and frequency caused by differences in receiver coupling at receivers $\mathbf{x}_i$ and $\mathbf{x}_j$, respectively; and $N(\mathbf{x}_i,\omega)$ and $N(\mathbf{x}_j,\omega)$ are the noises recorded at receivers $\mathbf{x}_i$ and $\mathbf{x}_j$.

First, we only consider the influence of amplitude variation among traces in the receiver-ground-coupling functions and ignore the noise term $N(\mathbf{x}_k,\omega)$. In this case, $R(\mathbf{x}_i,\omega)$ and $R(\mathbf{x}_j,\omega)$ are real values, and then equations 12–14 become

$$C_{ij}=|W(\omega)|^2R(\mathbf{x}_i,\omega)R(\mathbf{x}_j,\omega)G^*(\mathbf{x}_i,\omega)G(\mathbf{x}_j,\omega), \tag{17}$$

$$D_{ij}=\frac{R(\mathbf{x}_j,\omega)}{R(\mathbf{x}_i,\omega)}\frac{G^*(\mathbf{x}_i,\omega)G(\mathbf{x}_j,\omega)}{|G(\mathbf{x}_i,\omega)|^2}, \tag{18}$$

$$H_{ij}=\frac{G^*(\mathbf{x}_i,\omega)G(\mathbf{x}_j,\omega)}{|G(\mathbf{x}_i,\omega)||G(\mathbf{x}_j,\omega)|}. \tag{19}$$

All three methods provide the same phase information, but deconvolution and cross-coherence are independent of the source signature. If there is no amplitude variation among traces, that is $R(\mathbf{x}_i, \omega) = R(\mathbf{x}_j, \omega)$, the deconvolution and cross-coherence provide results with higher resolution than crosscorrelation does. Otherwise, only cross-coherence can remove the influence of amplitude variations and achieve a stable amplitude without additional processing to normalize the amplitude of traces constructed by interferometry.

Nakata et al. (2011) demonstrate that additive random noise causes an inconsequential bias in the cross-coherence, but the relative statistical uncertainty in the cross-coherence is reduced by a factor of $1/\sqrt{2}$ compared with crosscorrelation and deconvolution. Thus, in addition to treating the problem of anomalous trace amplitudes, cross-coherence is more stable in the presence of noise. The detailed proof can be found in Nakata et al. (2011).

RESULTS

We use synthetic and field data sets to demonstrate the equivalence of the conventional ICCM and ATRI methods, as well as the equivalence of the newly proposed cross-coherence migration and its corresponding ATRI method. We also compare the proposed method with conventional ICCM and deconvolution migration on imaging single source and multiple sources with true and perturbed velocity models. We further illuminate the spatially high-resolution property and the antinoise capability of the cross-coherence-based methods over crosscorrelation- and deconvolution-based methods using synthetic and field data.

Synthetic data tests

We use 2D acoustic finite-difference modeling data to illustrate the equivalence of the ICCM and ATRI methods and the improvements of the cross-coherence-based method over the crosscorrelation- and deconvolution-based methods. A part of the Marmousi II model (Martin et al., 2002) is used to introduce some complexity into the numerical experiments (Figure 2a). The part of the model we use is 11.2–13.4 km in the horizontal axis and 5.1–7.7 km in the vertical axis of the P-wave velocities of the Marmousi II model. A seismic source located at (2.0, 1.5) km, shown with a yellow cross in Figure 2a, is just below the high-velocity layer. The source time function is a Ricker wavelet with central frequency of 20 Hz. A total of 100 receivers with spatial interval of 40 m are placed at the surface to record seismic waves. Figure 2b shows the synthetic seismic data without noise. To demonstrate noise-resistant characteristics of the proposed methods, we add a different amount of band-limited random noise to each trace of the synthetic data. The relative amplitude among the traces is highly variable from trace to trace (Figure 2c). The S/N of the noisy data is −11.2 dB, where S/N is defined as $10\log_{10}E_{\text{signal}}/E_{\text{noise}}$ and E is the stacking power of a signal or noise.

First, we verify the equivalence of the ICCM and ATRI methods. Figure 3 compares the source images generated by the ICCM (the left column) and ATRI (the middle column) methods with and without velocity errors. The right column in Figure 3 shows the scale-up differences between ICCM and ATRI. From these images, we can see that the source images focus well even when the velocity is wrong. The reason is that autocorrelation always has a maximum at zero time lag. We also observe that the focused source moves downward (upward) when the velocity model is too slow (fast). From the scale-up differences (the right column in Figure 3) between the results produced by these two methods, we can see that ICCM and ATRI produce the same images regardless of the velocity model being correct or not.

Likewise, we also compare the source images made by the cross-coherence migration and corresponding improved ATRI method, as shown in Figure 4. Compared with the crosscorrelation-based methods, cross-coherence migration and its corresponding ATRI method produce source images with similar sensitivity to velocity errors, but with much higher spatial resolution. From the scale-up differences between the cross-coherence migration and its corresponding ATRI results (the right column in Figure 4), we confirm that these two methods are also equivalent. Note that the image differences in Figure 4 seem to be slightly larger than those shown in Figure 3. Such differences come from the stability factors introduced in the numerical division of cross-coherence-based methods.

Second, we compare the spatial resolution of source images provided by the crosscorrelation-, deconvolution-, and cross-coherence-based source location methods. Due to the equivalence, we only analyze the interferometric migration results in this test and the corresponding ATRI methods should share the same properties. Figure 5 shows the virtual shot gathers generated by crosscorrelation, deconvolution, and cross-coherence, respectively. The virtual shot (or master trace) is located at 1.44 km on the surface with the position marked by the vertical dashed line in Figure 5. We observe that deconvolution and cross-coherence greatly improve the temporal resolution of the virtual shot gathers. Moreover, cross-coherence provides slightly more balanced traces at the far offset than deconvolution does, as denoted by the red arrows in Figure 5. Figure 6

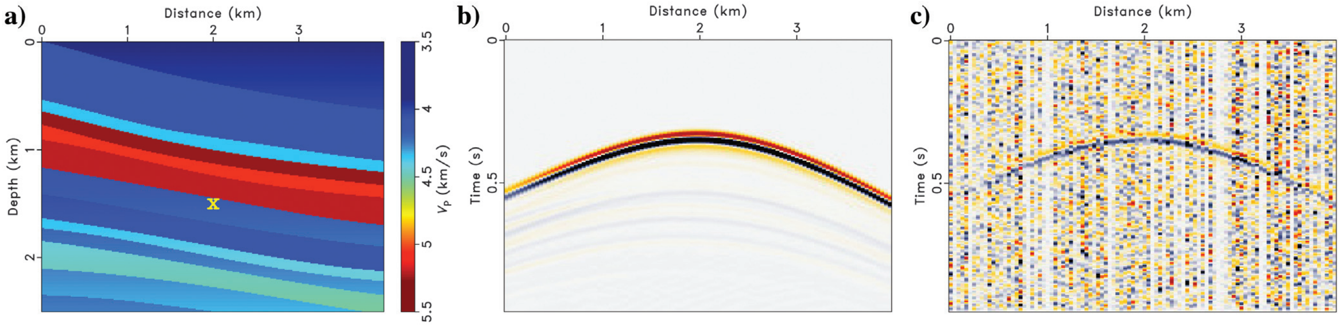

Figure 2. (a) Acoustic velocity model (a part of the Marmousi II model). The yellow cross indicates the location of the source. The receivers are deployed on the surface. (b) Synthetic shot gather without noise and (c) synthetic shot gather with highly variable random noise (S/N = −11.2 dB).

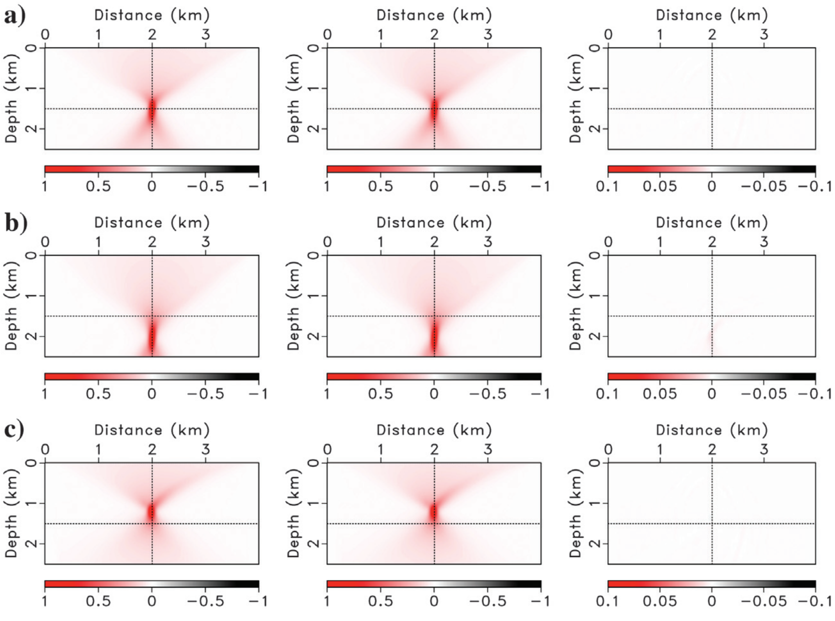

Figure 3. Comparisons of the ICCM and ATRI methods using (a) correct velocity, (b) 20% slower velocity, and (c) 20% faster velocity. The left column shows the ICCM images, the middle column shows the ATRI results, and the right column shows the differences between the ICCM images and ATRI results. The intersection of the black dotted lines indicates the true source location. Note that the scale of the color bar in the right column is only 10% of that in the left and middle columns.

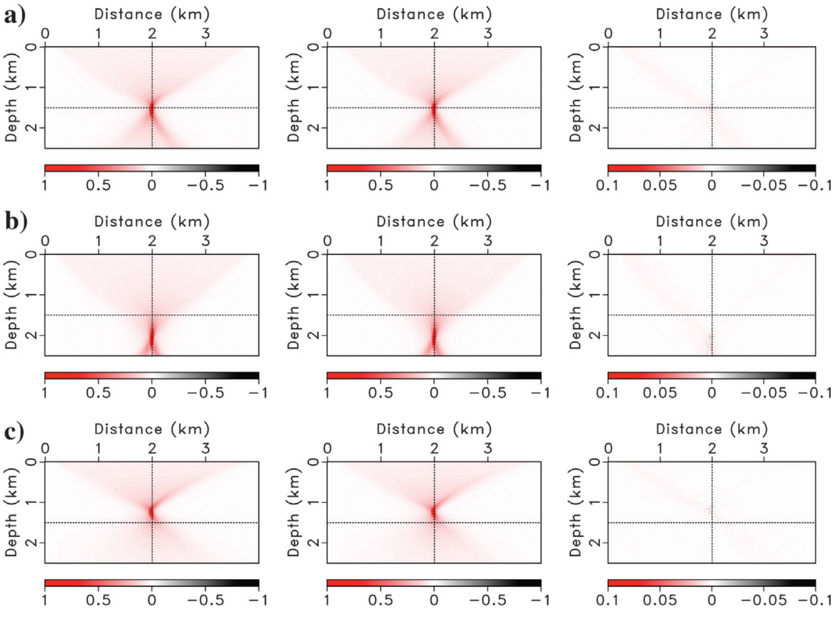

Figure 4. Comparisons of cross-coherence migration and its corresponding ATRI method using (a) correct velocity, (b) 20% slower velocity, and (c) 20% faster velocity. The left column shows the cross-coherence migration images, the middle column shows the cross-coherence-based ATRI results, and the right column shows the differences between cross-coherence migration and cross-coherence-based ATRI results. The intersection of the black dotted lines indicates the true source location. Note that the scale of the color bar in the right column is only 10% of that in the left and middle columns.

compares the source images using only one trace located at $x = 0.36$ km in the virtual shot gathers shown in Figure 5. The correct velocity model is used in this single-trace imaging test. We can see clearly that deconvolution and cross-coherence migration results have higher spatial resolution than the conventional ICCM method. Figure 7 compares the final stacked source images by these three methods. In this test, each master trace and its neighbors within 0.48 km are muted in the virtual shot gather during migration. The muting offset parameter is determined by trial and error and is well-tuned according to the image resolution and quality. Figure 7a–7c compares the close-up source images generated by the three methods with the true, 20% slower, and 20% faster velocities. We can see that deconvolution and cross-coherence migration produce similar results, which have much higher resolution than crosscorrelation migration does, regardless of whether correct or erroneous velocities are used. White noise is added to ensure the stability of deconvolution and cross-coherence. More specifically, white noise with 0.1% amplitude of the average power spectrum of the master trace is added in deconvolution and white noise with 0.1% amplitude of the average amplitude of the denominator in equation 10 is added in cross-coherence in the frequency domain.

Furthermore, we test the robustness of the crosscorrelation-, deconvolution-, and cross-coherence-based source location imaging methods in the presence of strong band-limited random noise, as shown in Figure 2c. Figure 8 compares the virtual shot gathers generated by crosscorrelation, deconvolution, and cross-coherence, respectively. Among these methods, cross-coherence gives the best virtual shot gathers in terms of S/N and trace balance. In this test, we also mute the master trace and its nearest neighbors with an offset of less than 0.48 km in each virtual shot gather before migration. Then, we perform migration to all of the virtual shot gathers. Figure 9 shows the imaging results generated using these three types of virtual shot gathers (Figure 8a–8c) with correct, 20% slower, and 20% faster velocities. These results demonstrate that the image resolution is slightly improved in the deconvolution method, but the cross-coherence method provides exceptionally clear and focused images with the highest S/N whether the velocity is correct or not. To ensure the stability of deconvolution and cross-coherence, here we add white noise, which has a 1% amplitude of the average power spectrum of the master trace in deconvolution and a 1% amplitude of the average amplitude of the denominator in equation 10 in cross-coherence in the frequency domain.

Finally, we perform a multisource location experiment on the same Marmousi II model.

The acquisition system retains the same parameters as in the first single source example. There are three sources under high-velocity layers as shown in Figure 10a with yellow crosses. They are distributed evenly from $x = 1.8$ km to $x = 2.2$ km with spacing of 258 m, where x is the horizontal coordinate. These sources from left to right act at the times 0.05, 0.1, and 0.2 s, respectively. Their source functions are Ricker wavelets with the same amplitude and frequency range. Because the average velocity above the sources is approximately 5 km/s and the central frequency of the wavelet is 20 Hz, the estimated wavelength is approximately 250 m, which is similar to the source spacing. Figure 10b shows the finite-difference modeled data. Different amounts of random noise are added to each trace of the synthetic data, as shown in Figure 10c. The S/N of the noisy data is -3.7 dB. Like the previous procedure used in the single-source location experiment, we mute the master trace and its nearest neighbors with an offset less than 0.48 km. Figure 11 shows the source images produced by the crosscorrelation migration, deconvolution migration, and cross-coherence migration methods with correct, 20% slower, and 20% faster velocities. Compared with the crosscorrelation- and

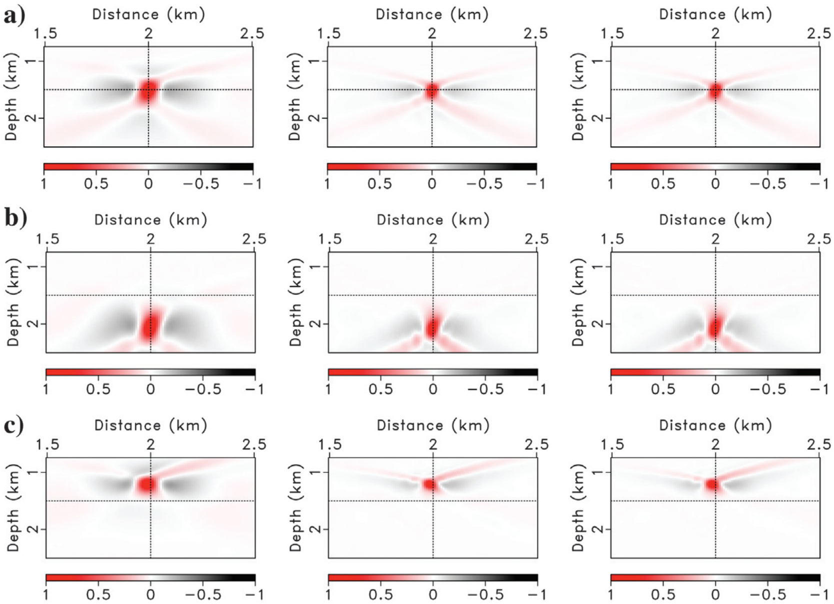

Figure 7. Close-up resolution comparisons of source images. Panels (a), (b), and (c) correspond to the correct velocity, 20% slower velocity, and 20% faster velocity, respectively. The left column shows the crosscorrelation migration results, the middle column shows the deconvolution migration results, and the right column shows the cross-coherence migration results. The intersection of the black dotted lines indicates the true source location.

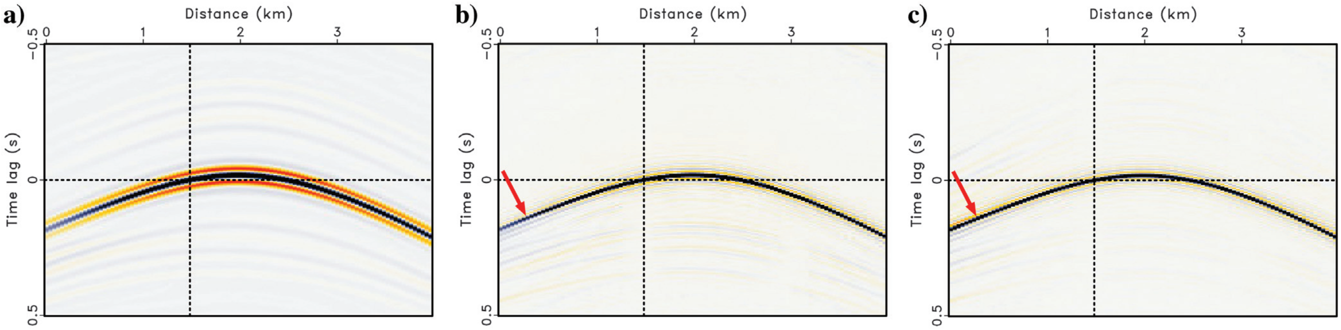

Figure 5. Virtual shot gathers using the noise-free data as input and generated by (a) crosscorrelation, (b) deconvolution, and (c) cross-coherence. The positions of the virtual shots are denoted by the vertical dash lines. Note the difference between (b) and (c) as pointed out by the red arrows.

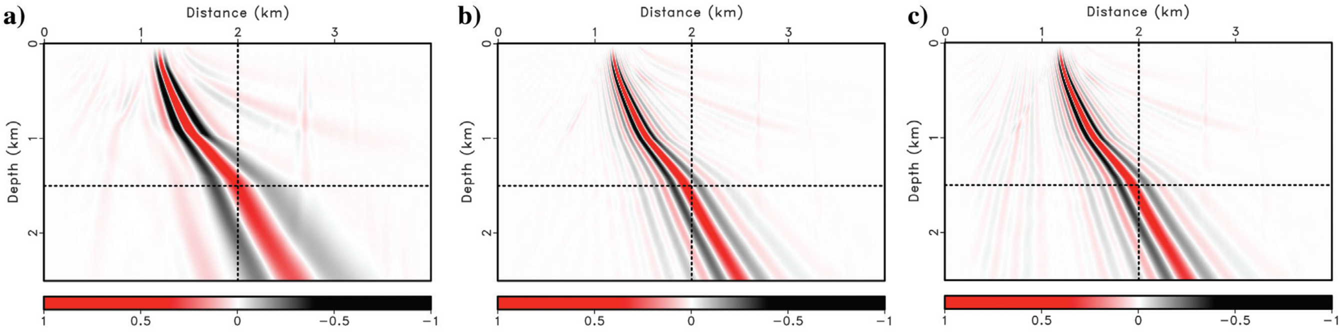

Figure 6. Source images using only one trace as input and generated by (a) crosscorrelation migration, (b) deconvolution migration, and (c) cross-coherence migration.

deconvolution-based methods, the cross-coherence-based method is the most robust one and can detect multiple sources simultaneously even in the presence of strong noises. To ensure the stability of deconvolution and cross-coherence, here we add white noise, which has a 1% amplitude of the average power spectrum of the master trace in deconvolution and a 1% amplitude of the average amplitude of the denominator in equation 10 in cross-coherence in the frequency domain.

Field data tests

We demonstrate the equivalence and effectiveness of the proposed methods with field data recorded on a 2D geophone array, which is part of the 3D acquisition geometry specially designed for a seismic while drilling (SWD) trial test in the Middle East. In this SWD test, seismic signals generated by the drill bit are recorded passively by the seismic sensors on the surface while drilling. One purpose of this test is to locate the relative position of the drill bit on the subsurface seismic image produced by depth migration of seismic data recorded on the surface, and then the subsurface seismic image can be used for real-time drilling navigation. One key step of data preprocessing is to extract the drill-bit signature (or, namely, the pilot trace) from responses recorded on dedicated reference sensors at the top of the drilling string (near the swivel). Then, a sequence of seismic traces is generated by continuously correlating the pilot with the data recorded on the surface sensors (Rector and Marion, 1991; Poletto and Miranda, 2004).

Figure 12a shows the 1D velocity model used for source imaging. The model is estimated from a vertical seismic profile survey. Figure 12b shows the preprocessed shot gather, which is generated from 1 h long recordings. The preprocessing steps involve producing a pilot trace with time-delay correlation, deconvolving the geophone data with the pilot trace, and 3D-to-2D conversion by multiplying the data spectra by $\sqrt{i/\omega}$ and then gaining in the time domain by $\sqrt{t}$ (Barton, 1989). The offset ranges from −1.6 to 1.6 km, and the receiver spacing interval is 25 m. The minimum offset is 75 m because the near offsets are not accessible in the field acquisition. Because only the direct wave is needed to estimate the source location, we extract it from the preprocessed data by windowing out all but the direct arrival, as denoted by the red arrows in Figure 12b. Additionally a slope-based filter is applied to the windowed data to improve the event continuity. The extracted direct wave is shown in Figure 12c. Figure 13 shows the virtual shot gathers generated by the crosscorrelation, deconvolution, and cross-coherence methods, respectively. The virtual shot locates at the position of offset −0.6 km, as shown by the vertical dashed lines in Figure 13. From the comparisons, we can see that cross-coherence produces the best virtual shot gather in terms of S/N and temporal resolution.

Then, we use the processed field data to verify the equivalence of the ICCM and ATRI methods, as well as the equivalence of the proposed cross-coherence migration and its corresponding ATRI method. Figure 14a and 14b displays the source images generated by the crosscorrelation migration and ATRI methods. After comparing these two results and computing their differences, as shown in

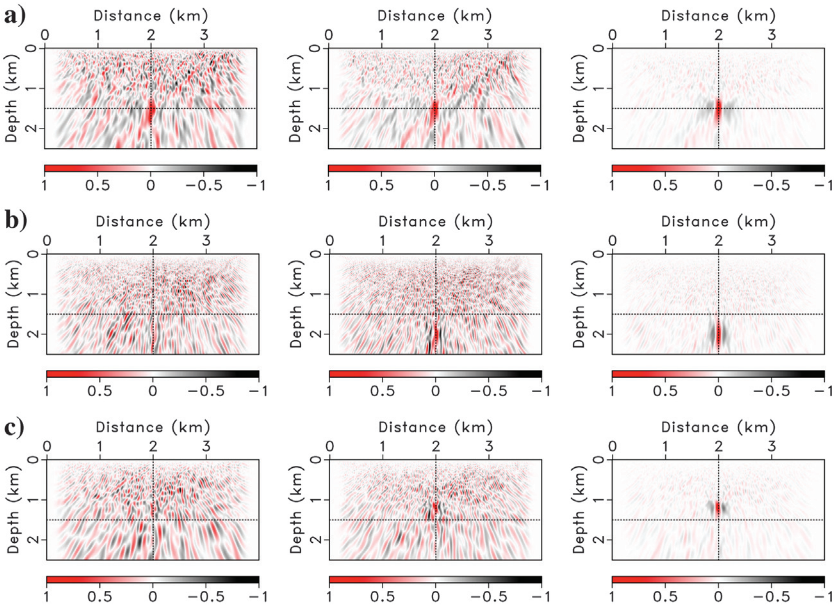

Figure 9. Noise-resistant comparisons of the crosscorrelation migration, deconvolution migration, and cross-coherence migration methods using the (a) correct velocity, (b) 20% slower velocity, and (c) 20% faster velocity. The left column shows the crosscorrelation migration results, the middle column shows the deconvolution migration results, and the right column shows the cross-coherence migration results. The intersection of the black dotted lines indicates the true source location.

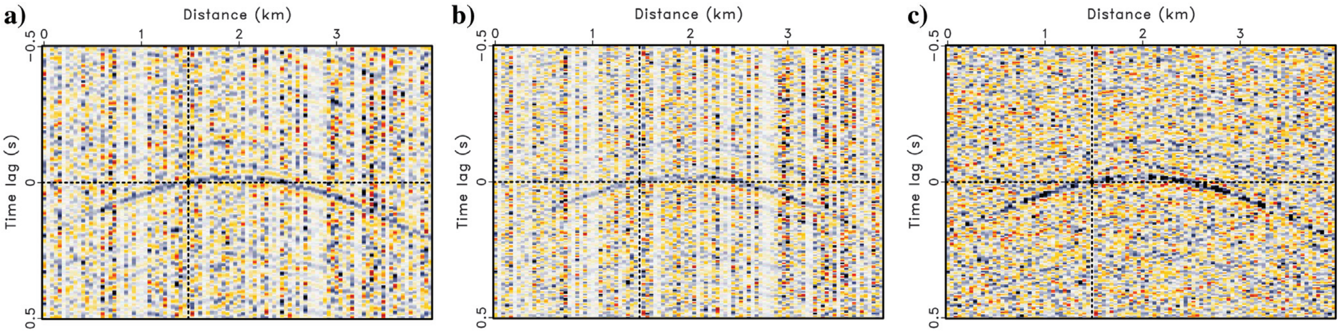

Figure 8. Virtual shot gathers using the noisy data as input and generated by (a) crosscorrelation, (b) deconvolution, and (c) cross-coherence. The positions of the virtual shots are denoted by the vertical dashed lines.

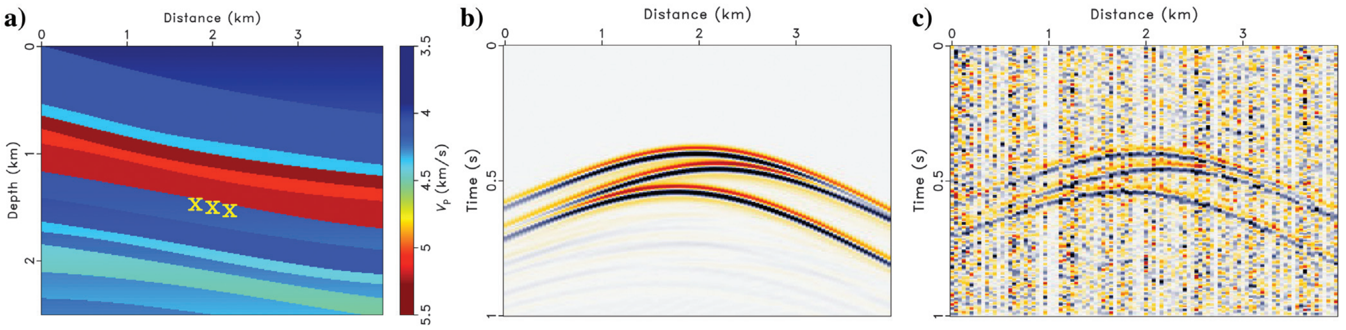

Figure 10. (a) Acoustic velocity model (a part of the Marmousi II model). The yellow crosses on the velocity model indicate the true locations of the multisources. The receivers are deployed on the surface. Recorded seismic data (b) without noise and (c) with −3.7 dB noise.

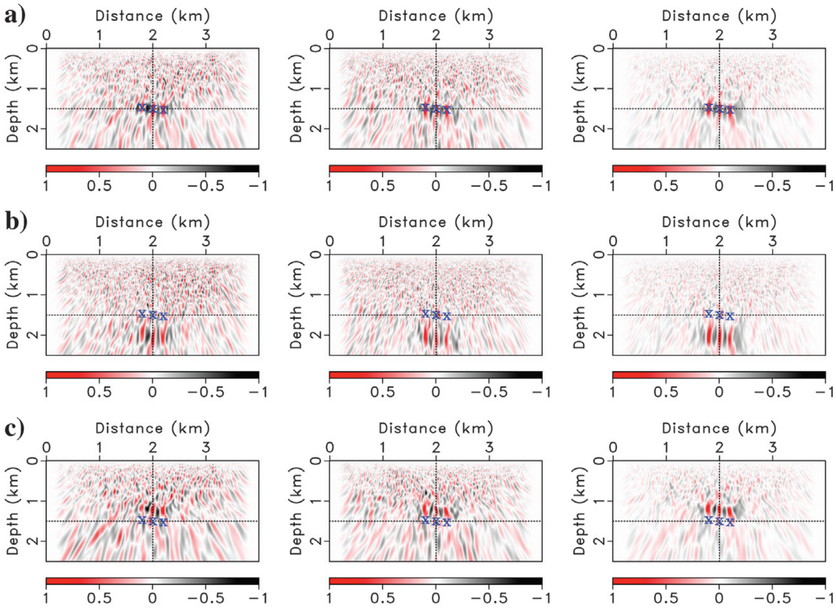

Figure 11. Noise-resistant comparisons of multisource images produced by crosscorrelation migration, deconvolution migration, and cross-coherence migration methods using the (a) correct velocity, (b) 20% slower velocity, and (c) 20% faster velocity. The left column shows the crosscorrelation migration results, the middle column shows the deconvolution migration results, and the right column shows the cross-coherence migration results. The blue crosses indicate the true source locations.

Figure 14c, we can see that these two methods are equivalent. We also apply cross-coherence migration and its corresponding ATRI implementation to obtain the source images, as shown in Figure 15a and 15b. The difference is shown in Figure 15c. From these figures, we can verify that the proposed cross-coherence migration and its corresponding ATRI methods are also identical.

Finally, we compare the image resolution of the crosscorrelation migration, deconvolution migration, and cross-coherence migration. In this test, the trace at the master trace location and its nearest neighbors with an offset of less than 0.2 km are muted. The muting offset parameter is determined by trial and error and is well-tuned according to the image resolution and quality. Figure 16a–16c shows the close-up source images produced by crosscorrelation migration, deconvolution migration, and cross-coherence migration, respectively. To illuminate the uncertainty of source locating methods due to noises and the resolution limitations, we normalize each source image and overlay the contour of $I(\mathbf{x}) = 0.7$ in a blue ring. The true location of the drill bit is at the cross point of the horizontal and vertical dashed lines in Figure 16a–16c. Comparing

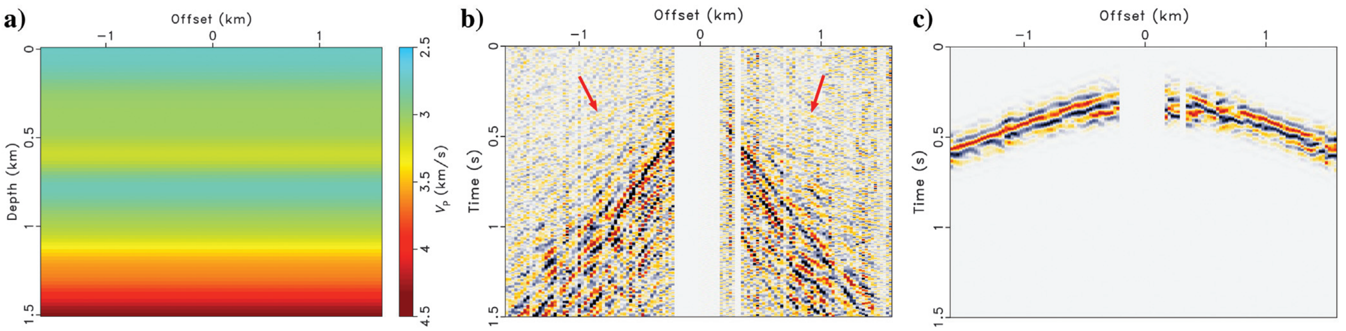

Figure 12. (a) Velocity model and (b) preprocessed data. The direct wavefield is hardly visible, as denoted by the red arrows. (c) Extracted direct wavefield.

these three images, cross-coherence migration produces source image with the least uncertainty on the drill-bit location. For more details, Figure 16d and 16e shows the vertical and horizontal traces crossing at the maximum amplitudes of each image. From these results, we can see that the source image provided by the cross-coherence migration has the highest spatial resolution and is contaminated by the noise to the least extent. To ensure the stability of deconvolution and cross-coherence, here we add white noise, which has a 0.1% amplitude of the average power spectrum of the master trace in deconvolution and a 0.1% amplitude of the average amplitude of the denominator in equation 10 in cross-coherence in the frequency domain.

DISCUSSION

Compared with the interferometric crosscorrelation migration, deconvolution migration and cross-coherence migration improve the spatial resolution of the source image. In the deconvolution approach, some level of white noise has to be added to prevent numerical instability. If we choose a regularization parameter that is too large, the regularized deconvolution reduces to crosscorrelation. However, if the regularization parameter is too small, the deconvolution is unstable. Although instability also occurs in cross-coherence, in practice, we can choose a much smaller regularization parameter because the numerator and denominator are small when the spectral amplitude is

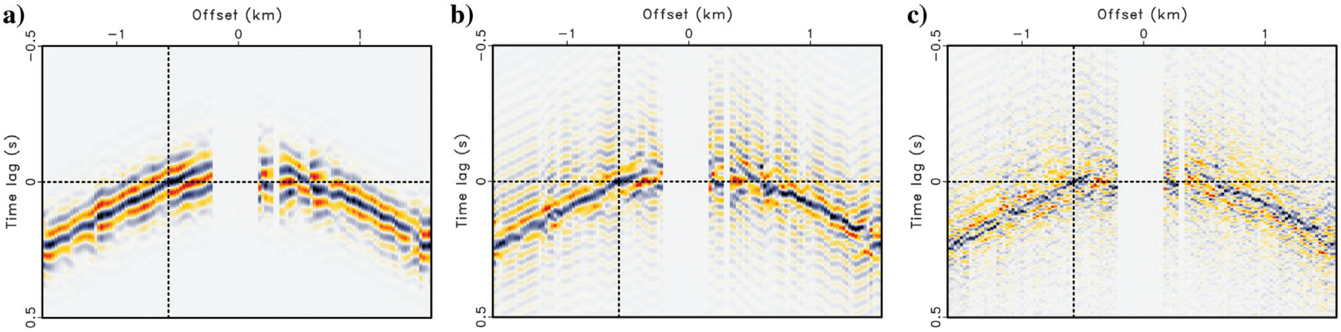

Figure 13. Virtual shot gathers generated by (a) crosscorrelation, (b) deconvolution, and (c) cross-coherence.

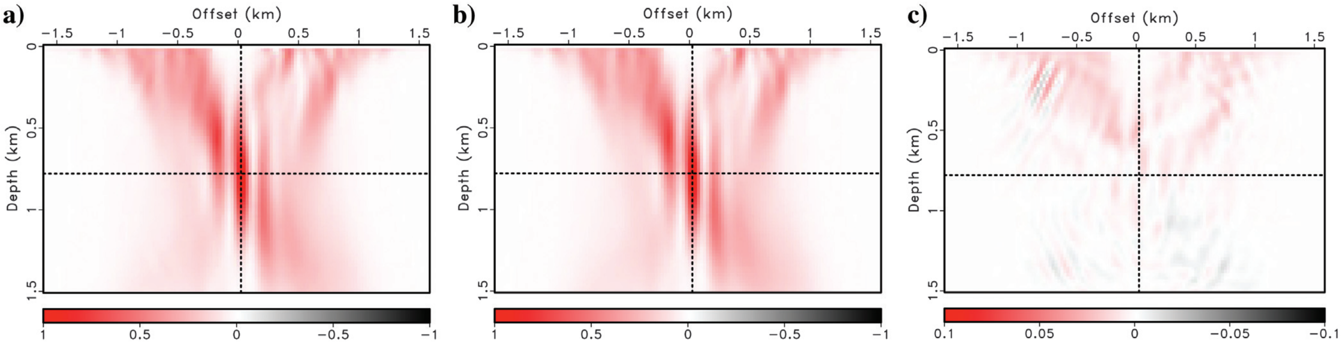

Figure 14. Source images with the (a) ICCM method and (b) ATRI method and (c) the difference between (a) and (b). Note that the scale of the color bar in (c) is only 10% of that in (a) and (b).

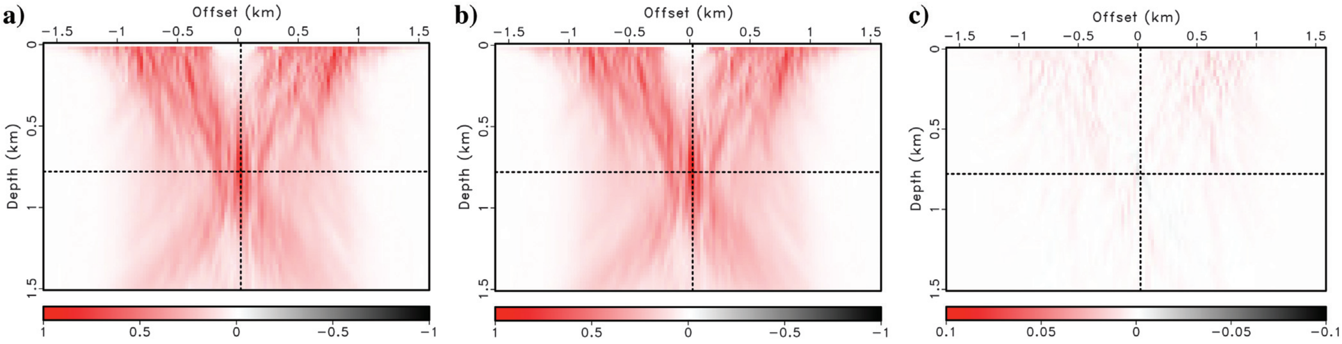

Figure 15. Source images with (a) cross-coherence migration and (b) cross-coherence-based ATRI method and (c) the difference between (a) and (b). Note that the scale of the color bar in (c) is only 10% of that in (a) and (b).

small. Moreover, compared with the deconvolution method, cross-coherence removes the influence of amplitude variations and achieves a stable amplitude without separate processing to normalize the amplitude of traces constructed by interferometry. In addition, it is possible to further improve the spatial resolution of the source image by least-squares inversion, especially with the sparse constraint on the source distribution (Gao et al., 2017; Sharan et al., 2018; Li et al., 2019).

Even though we have demonstrated that the proposed cross-coherence migration and its corresponding ATRI method are capable of producing high-resolution focused source images, the results have a high dependency on velocity accuracy. Single-source and multiple-source examples show incorrect locations of the focused energy in the presence of velocity errors. Extended imaging conditions for passive seismic data can be used to evaluate the focusing of a given event and test the accuracy of the velocity model (Witten and Shragge, 2015; Nakata, 2018). Moreover, the extended imaging conditions can be used to invert for the P- and S-wave velocity models through the full-wavefield adjoint-state method (Witten and Shragge, 2017a, 2017b). Most velocity inversion methods using passive seismic data need to first locate the sources at each iteration of velocity updates (Wang and Alkhalifah, 2018; Song et al., 2019). Thus, the cross-coherence-based methods will be beneficial for the velocity estimation because they can provide source images with high resolution even in the case of data having very low S/N. This subject is beyond the scope of this paper and remains to be explored in the near future.

Because microseismic data inherently contain P- and S-waves, another future work is to extend the proposed cross-coherence migration and its corresponding ATRI method to the elastic case. The straightforward approach might be separating the P- and S-components of the wavefield before applying the proposed methods. However, this approach depends on how well we can separate the P- and S-wave from the data, which may be challenging in complex media and general geometry (Li et al., 2018). Another approach is to preprocess the multicomponent data by cross-coherence or spectral whitening and then extrapolate the entire preprocessed elastic wavefields followed by wave-mode separation and imaging condition. Compared to the first approach, wavefield decomposition instead is performed after extrapolation in the image domain that enjoys more regular sampling and a complete depth axis. However, cross-coherence and spectral whitening introduce interference terms when there is more than one event in the data (Nakata et al., 2011), which is often the case for multicomponent data. Work is underway to fully investigate the effects of these additional interference terms on the source imaging.

CONCLUSION

We have proven theoretically that ICCM is equivalent to the zero-lag ATRI method. Synthetic and field data tests confirm the theoretical result. It is not only important from a theoretical point of view, but it has a direct application to 3D source imaging projects. Because the results produced by ICCM and ATRI are the same, the choice between these two methods might depend on other practical considerations, such as relative efficiency and flexibility.

Besides showing the equivalence of ICCM and ATRI, we proposed two new source-locating approaches based on the cross-coherence method. The first one is similar to the conventional cross-correlation migration method, except we replace crosscorrelation with cross-coherence for generating virtual shot gathers. The second approach applies frequency normalization to the input data and then generates the source image by zero-lag autocorrelation of the time-reversal wavefield reconstructed from the normalized data. Likewise, the two modified ICCM and ATRI approaches are theoretically equivalent, which also is verified by synthetic and field data tests. We further compared the proposed methods with conventional ICCM and deconvolution migration under different conditions including

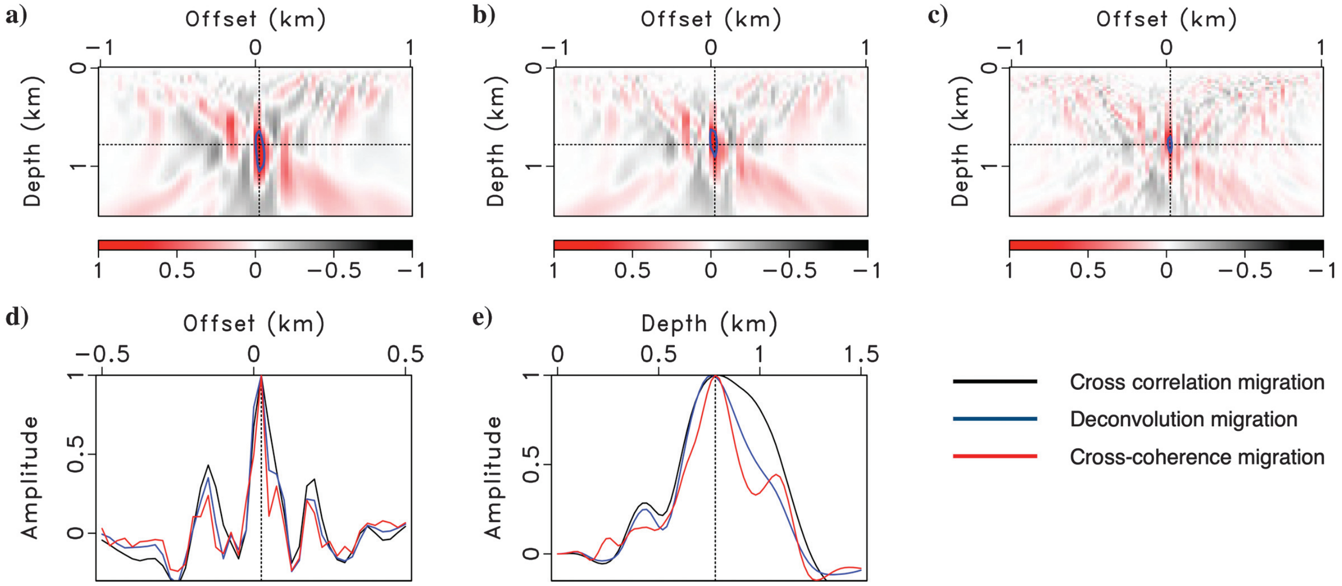

Figure 16. Close-up comparisons of source images produced by (a) crosscorrelation migration, (b) deconvolution migration, and (c) cross-coherence migration. The blue ring in each image displays a contour with $I(\mathbf{x}) = 0.7$ after image normalization. (d) Amplitudes of the images at a fixed depth and (e) amplitudes of the images at a fixed offset. The fixed depth and distance are shown by the horizontal and vertical dashed lines in (a), (b), and (c).

band-limited random noise, velocity perturbations, and multiple sources. Test results demonstrate that the proposed methods improve the spatial resolution of the source image and are particularly effective and robust in the presence of highly variable and strong additive random noise.

ACKNOWLEDGMENTS

The authors thank Saudi Aramco for the permission to publish this paper. We thank the editors J. Shragge, A. Cheng, and Y. Liu and three anonymous reviewers for their valuable suggestions.

DATA AND MATERIALS AVAILABILITY

Data associated with this research are confidential and cannot be released.

REFERENCES

Aki, K., 1957, Space and time spectra of stationary stochastic waves, with special reference to microtremors: Bulletin of the Earthquake Research Institute, University of Tokyo, **35**, 415–456.

Artman, B., 2006, Imaging passive seismic data: Geophysics, **71**, no. 4, SI177–SI187, doi: 10.1190/1.2209748.

Artman, B., I. Podladtchikov, and B. Witten, 2010, Source location using time-reverse imaging: Geophysical Prospecting, **58**, 861–873, doi: 10.1111/j.1365-2478.2010.00911.x.

Barton, G., 1989, Elements of Green's functions and propagation: potentials, diffusion, and waves: Oxford University Press.

Cao, W., S. M. Hanafy, G. T. Schuster, G. Zhan, and C. Boonyasiriwat, 2012, High-resolution and super stacking of time-reversal mirrors in locating seismic sources: Geophysical Prospecting, **60**, no. 1, 1–17, doi: 10.1111/j.1365-2478.2011.00957.x.

Claerbout, J. F., 1971, Toward a unified theory of reflector mapping: Geophysics, **36**, no. 3, 467–481, doi: 10.1190/1.1440185.

Douma, J., R. Snieder, A. Fish, and P. Sava, 2013, Locating a microseismic event using deconvolution: 83rd Annual International Meeting, SEG, Expanded Abstracts, 2206–2211, doi: 10.1190/segam2013-0446.1.

Fink, M., 2006, Time-reversal acoustics in complex environments: Geophysics, **71**, no. 4, SI151–SI164, doi: 10.1190/1.2215356.

Gajewski, D., and E. Tessmer, 2005, Reverse modelling for seismic event characterization: Geophysical Journal International, **163**, 276–284, doi: 10.1111/j.1365-246X.2005.02732.x.

Gao, W., M. Sacchi, and Z. Li, 2017, Microseismic-source location via elastic least-squares full-waveform inversion with a group sparsity constraint: 87th Annual International Meeting, SEG, Expanded Abstracts, 2814–2819, doi: 10.1190/segam2017-17785680.1.

Girard, A.J., and J. Shragge, 2020, Direct migration of ambient seismic data: Geophysical Prospecting, **68**, 270–292, doi: 10.1111/gpr.v68.1.

Kao, H., and S. J. Shan, 2004, The source-scanning algorithm: Mapping the distribution of seismic sources in time and space: Geophysical Journal International, **157**, 589–594, doi: 10.1111/j.1365-246X.2004.02276.x.

Li, E. Y., and M. van der Baan, 2016, Microseismic event localization by acoustic time reversal extrapolation: Geophysics, **81**, no. 3, KS123–KS134, doi: 10.1190/geo2015-0300.1.

Li, E. Y., Y. Du, J. Yang, A. Cheng, and X. Fang, 2018, Elastic reverse time migration using acoustic propagators: Geophysics, **83**, no. 5, S399–S408, doi: 10.1190/geo2017-0687.1.

Li, F., Y. Qin, and W. Song, 2019, Waveform inversion-assisted distributed reverse time migration for microseismic location: IEEE Journal of Selected Topics in Applied Earth Observations and Remote Sensing, **12**, 327–1332, doi: 10.1109/JSTARS.2019.2904206.

Martin, G. S., K. J. Marfurt, and S. Larsen, 2002, Marmousi-2: An update model for the investigation of AVO in structurally complex area: 72nd Annual International Meeting, SEG, Expanded Abstracts, 1979–1982, doi: 10.1190/1.1817083.

Maxwell, S. C., J. Rutledge, R. Jones, and M. Fehler, 2010, Petroleum reservoir characterization using downhole microseismic monitoring: Geophysics, **75**, no. 5, 75A129–75A137, doi: 10.1190/1.3477966.

McMechan, G. A., 1982, Determination of source parameters by wavefield extrapolation: Geophysical Journal International, **71**, 613–628, doi: 10.1111/j.1365-246X.1982.tb02788.x.

Nakata, N., 2018, Extended imaging conditions for passive seismic data with GmRTM: 88th Annual International Meeting, SEG, Expanded Abstracts, 2957–2961, doi: 10.1190/segam2018-2998514.1.

Nakata, N., and G. C. Beroza, 2016, Reverse time migration for microseismic sources using the geometric mean as an imaging condition: Geophysics, **81**, no. 2, KS51–KS60, doi: 10.1190/geo2015-0278.1.

Nakata, N., R. Snieder, T. Tsuji, K. Larner, and T. Matsuoka, 2011, Shear wave imaging from traffic noise using seismic interferometry by cross-coherence: Geophysics, **76**, no. 6, SA97–SA106, doi: 10.1190/geo2010-0188.1.

Poletto, F. B., and F. Miranda, 2004, Seismic while drilling: Fundamentals of drill-bit seismic for exploration (Vol. 35): Elsevier.

Pujol, J., 2004, Earthquake location tutorial: graphical approach and approximate epicentral location techniques: Seismological Research Letters, **75**, 63–74, doi: 10.1785/gssrl.75.1.63.

Rector, J. W., III, and B. P. Marion, 1991, The use of drill-bit energy as a downhole seismic source: Geophysics, **56**, 628–634, doi: 10.1190/1.1443079.

Sava, P., 2011, Micro-earthquake monitoring with sparsely sampled data: Journal of Petroleum Exploration and Production Technology, **1**, 43–49, doi: 10.1007/s13202-011-0005-7.

Schuster, G. T., J. Yu, J. Sheng, and J. Rickett, 2004, Interferometric/daylight seismic imaging: Geophysical Journal International, **157**, 838–852, doi: 10.1111/j.1365-246X.2004.02251.x.

Shapiro, S., 2015, Fluid-induced micro seismicity: Cambridge University Press.

Sharan, S., R. Wang, and F. J. Herrmann, 2018, Fast sparsity-promoting microseismic source estimation: Geophysical Journal International, **216**, 164–181, doi: 10.1093/gji/ggy415.

Snieder, R., A. Grêt, H. Douma, and J. Scales, 2002, Coda wave interferometry for estimating nonlinear behavior in seismic velocity: Science, **295**, 2253–2255, doi: 10.1126/science.1070015.

Song, C., T. Alkhalifah, and Z. Wu, 2019, Microseismic event estimation and velocity analysis based on a source-focusing function: Geophysics, **84**, no. 3, KS85–KS94, doi: 10.1190/geo2018-0205.1.

Song, C., T. Alkhalifah, Z. Wu, and B. Sun, 2017, Nonstationary filter used in microseismic-source imaging: 87th Annual International Meeting, SEG, Expanded Abstracts, 2898–2902, doi: 10.1190/segam2017-17658444.1.

Sun, J., Z. Xue, S. Fomel, T. Zhu, and N. Nakata, 2016, Full-waveform inversion of passive seismic data for sources and velocities: 86th Annual International Meeting, SEG, Expanded Abstracts, 1405–1410, doi: 10.1190/segam2016-13959115.1.

Sun, J., T. Zhu, S. Fomel, and W. Song, 2015, Investigating the possibility of locating microseismic sources using distributed sensor networks: 85th Annual International Meeting, SEG, Expanded Abstracts, 2485–2490, doi: 10.1190/segam2015-5888848.1.

Waldhauser, F., and W.L. Ellsworth, 2000, A double-difference earthquake location algorithm: Method and application to the northern Hayward fault, California: Bulletin of the Seismological Society of America, **90**, 1353–1368, doi: 10.1785/0120000006.

Wang, H., and T. Alkhalifah, 2018, Microseismic imaging using a source function independent full waveform inversion method: Geophysical Journal International, **214**, 46–57, doi: 10.1093/gji/ggy121.

Witten, B., and J. Shragge, 2015, Extended wave-equation imaging conditions for passive seismic data: Geophysics, **80**, no. 6, WC61–WC72, doi: 10.1190/geo2015-0046.1.

Witten, B., and J. Shragge, 2017a, Image-domain velocity inversion and event location for microseismic monitoring: Geophysics, **82**, no. 5, KS71–KS83, doi: 10.1190/geo2016-0561.1.

Witten, B., and J. Shragge, 2017b, Microseismic image-domain velocity inversion: Marcellus Shale case study: Geophysics, **82**, no. 6, KS99–KS112, doi: 10.1190/geo2017-0263.1.

Wu, S., Y. Wang, Y. Zheng, and X. Chang, 2017, Microseismic source locations with deconvolution migration: Geophysical Journal International, **212**, 2088–2115, doi: 10.1093/gji/ggx518.

Zhang, H., and C. H. Thurber, 2003, Double-difference tomography: The method and its application to the Hayward Fault, California: Bulletin of the Seismological Society of America, **93**, 1875–1889, doi: 10.1785/0120020190.

Zhao, Y., and A. Curtis, 2019, Relative source location using coda-wave interferometry: Method, code package, and application to mining-induced earthquakes: Geophysics, **84**, no. 3, F73–F84, doi: 10.1190/geo2018-0601.1.

Zhu, T., J. Sun, D. Gei, J. M. Carcione, P. Cance, and C. Huang, 2019, Hybrid multiplicative time-reversal imaging reveals the evolution of microseismic events: Theory and field-data tests. Geophysics, **84**, no. 3, KS71–KS83, doi: 10.1190/geo2018-0662.1.